Unsaturated selenium-enriched MoSe$_{2+x}$ amorphous nanoclusters: One-step photoinduced co-reduction route and its boosted photocatalytic H$_2$-evolution activity for TiO$_2$

Duoduo Gao [a], Jiachao Xu [a], Feng Chen [a], Ping Wang [a], Huogen Yu [a,b,*]

[a] State Key Laboratory of Silicate Materials for Architectures and School of Chemistry, Chemical Engineering and Life Sciences, Wuhan University of Technology, Wuhan 430070, PR China
[b] Laboratory of Solar Fuel, Faculty of Materials Science and Chemistry, China University of Geosciences, Wuhan 430074, PR China

ARTICLE INFO

ABSTRACT

Maximumly increasing the number of active sites is crucial to improve the H$_2$-evolution efficiency of cocatalyst. Herein, a rich-active-site regulation strategy by the synergism of unsaturated selenium enrichment and amorphization is developed to precisely construct unsaturated selenium-enriched MoSe$_{2+x}$ amorphous nanoclusters onto the TiO$_2$ via a mild photoinduced co-reduction route by using MoCl$_5$ and dibenzyl diselenide as the precursors. The resulting a-MoSe$_{2+x}$ exposes more unsaturated Se atoms (46.5%) because of its unsaturated Se-enriched configuration, highly irregular arrangement, and ultrasmall size (0.3 −1 nm). Photocatalytic tests show that the a-MoSe$_{2+x}$/TiO$_2$(3 wt%) achieves an optimal H$_2$-evolution rate (4984.46 μmol h^{-1} g^{-1}, AQE = 23.90%), with the 4.51-fold enhancement relative to that of c-MoSe$_2$/TiO$_2$. Hence, a rich unsaturated Se-mediated H$_2$-evolution mechanism is proposed, namely, the abundant unsaturated Se atoms as the active sites can not only provide sufficient proton-adsorption-centers to enrich H$^+$, but also present an outstanding catalytic efficiency to fleetly convert H$^+$ to H$_2$.

1. Introduction

Solar-driven photocatalytic H$_2$-evolution provides a promising way to alleviate the aggravated energy crisis and environmental deterioration [1–5]. However, most photocatalysts are still limited by the quick charge recombination and depressed interfacial H$_2$-evolution reaction [6–9]. Thus, various strategies of semiconductor coupling [10–12], cocatalyst modification [13–15], and morphological control [16] have been developed to as the effective approaches for solving the above issues. Among these, cocatalyst modification is one of the most efficient strategies to simultaneously suppress the charge recombination and improve the interfacial H$_2$-evolution rate [17,18]. In particular, precious metals (involving Pt, Au, Ag, and Ru) [19–22] have been extensively used to boost the H$_2$-evolution performance of various photocatalysts, while the high-cost and limited-reserves severely obstruct their practical use [23]. Therefore, it is urgent to exploit high-activity and low-cost cocatalysts for remarkably facilitating the performance of photocatalytic H$_2$-generation.

2D transition-metal selenides, especially molybdenum selenide (MoSe$_2$), have been considered as a capable candidate to replace noble metal for photocatalytic H$_2$-evolution due to the comparable Se−H$_{ads}$ (273 kJ/mol) [24] bond energy to Pt−H (251 kJ/mol) [25]. In addition, the theoretical study further confirmed that the unsaturated Se in the edge of MoSe$_2$ displays an analogous ΔG_{H*} to precious metal Pt [26,27], manifesting that the MoSe$_2$ with the excellent unsaturated edge Se sites can be used as the superior H$_2$-production cocatalyst. Unfortunately, the number of exposed edge unsaturated Se on crystalline MoSe$_2$ is very inadequate since the crystalline MoSe$_2$ usually present a large bulk (Fig. 1A), which severely hinders the exposure of edge unsaturated Se sites. Consequently, some researchers [28,29] have proved that the exfoliation of bulk MoSe$_2$ into 2D nanosheets can be identified as the feasible way to increase its edge unsaturated Se sites (Fig. 1B), while the increased degree is still quite limited because the inherent unsaturated Se sites are only distributed on the very few edges of crystalline MoSe$_2$. Actually, in comparison to the extensively used crystalline cocatalysts, the amorphous cocatalysts generally show a better activity because of its

---

isotropy and intrinsic disordered arrangement that are advantageous to expose numerous unsaturated active sites (both in the edge and interior) (Fig. 1C) [30,31]. In addition, the above unique structure endows amorphous cocatalyst with high structural flexibility, enabling the active sites to adopt suitable geometrical morphology (by dynamic surface self-reconstruction process) for activating H^+ or H_2O due to their unsaturation [32], finally improving the efficiency of a single active site for rapid H_2-evolution reaction. As a result, active-site regulation based on amorphization of crystalline materials has been proposed and verified to be an excellent strategy for enhancing the exposure of unsaturated active atoms, which has attracted extensive research. For example, Chang et al. reported that the amorphous MoS_x with more exposed unsaturated S sites has eight-fold higher H_2-generation rate than the crystalline MoS_2-deposited TiO_2 [31]. Moreover, the analogous result also exists in other amorphous chalcogenides (NiS_x, CoS_x, WS_x et al.) [4, 33]. Actually, in addition to the amorphization of H_2-evolution cocatalysts, the unsaturated selenium enrichment of cocatalysts (via selectively introducing target H_2-evolution active atoms) can also function as an effective approach for further increasing the number of H_2-generation active sites (Fig. 1D), which has been successfully conducted and confirmed in selenium-rich $a\text{-}NiSe_{1+x}$ [30], sulfur-rich $a\text{-}CoS_{1+x}$ [4], and tellurium-rich $a\text{-}NiTe_{1+x}$ systems [19]. However, there are currently no relevant reports on the construction of amorphous or/and unsaturated selenium-enriched $MoSe_{2+x}$ cocatalyst. Therefore, it is quite expected that the simultaneous incorporation of unsaturated selenium enrichment and amorphization in molybdenum selenide should become a rational idea to construct efficient unsaturated selenium-enriched $MoSe_{2+x}$ amorphous cocatalyst.

In this study, to maximize the number of unsaturated active Se atoms, a rich-active-site regulation strategy (by combining unsaturated selenium enrichment and amorphization) is proposed to manipulate unsaturated selenium-enriched $MoSe_{2+x}$ amorphous nanoclusters (termed $a\text{-}MoSe_{2+x}$). In this case, unsaturated Se-enriched $a\text{-}MoSe_{2+x}$

nanocluster, as an ingenious and robust H_2-evolution cocatalyst, can be elaborately produced and simultaneously integrated with TiO_2 by a mild photoinduced co-reduction route by using $MoCl_5$ and dibenzyl diselenide as the precursors. Interestingly, compared with the crystalline c-$MoSe_2$ (8.1%) and conventional amorphous a-$MoSe_2$ (24.9%), the a-$MoSe_{2+x}$ presented more unsaturated selenium (46.5%) owing to its unsaturated Se-enriched configuration, highly irregular arrangement, and smaller nanocluster (0.3–1 nm). As predicted, the resultant unsaturated selenium-enriched a-$MoSe_{2+x}$ can tremendously improve the photocatalytic H_2-evolution performance of TiO_2 (4984.46 μmol h^{-1} g^{-1}, AQE = 23.90%, λ = 365 nm), up to 4.51 and 1.76 times as high as that of crystalline c-$MoSe_2$/TiO_2 and conventional amorphous a-$MoSe_2$/ TiO_2 photocatalysts, respectively. Based on the above results, a rich unsaturated Se-mediated H_2-evolution mechanism is proposed, namely, the abundant unsaturated Se atoms as the active sites can not only provide sufficient proton-adsorption-centers to enrich H^+, but also present an outstanding catalytic efficiency to fleetly convert H^+ to H_2. It is worth mentioning that the a-$MoSe_{2+x}$ is proved to be versatile H_2-evolution cocatalyst on different photocatalysts, and the existing one-step photoinduced co-reduction method is also employed to prepare a series of selenide cocatalysts. The presented rich-active-site regulation strategy of unsaturated selenium enrichment and amorphization delivers a reliable idea to collectively increase the catalytic active site, which can inspire more insights into the design of active-site-enriched catalytic materials towards various applications.

2. Experimental sections

2.1. Synthesis of unsaturated selenium-enriched a-MoSe₂₊ₓ/TiO₂

The unsaturated selenium-enriched a-$MoSe_{2+x}$/TiO_2 photocatalyst was prepared via a mild photoinduced co-reduction route by using $MoCl_5$ and dibenzyl diselenide as the precursors. First, 50 mg of TiO_2
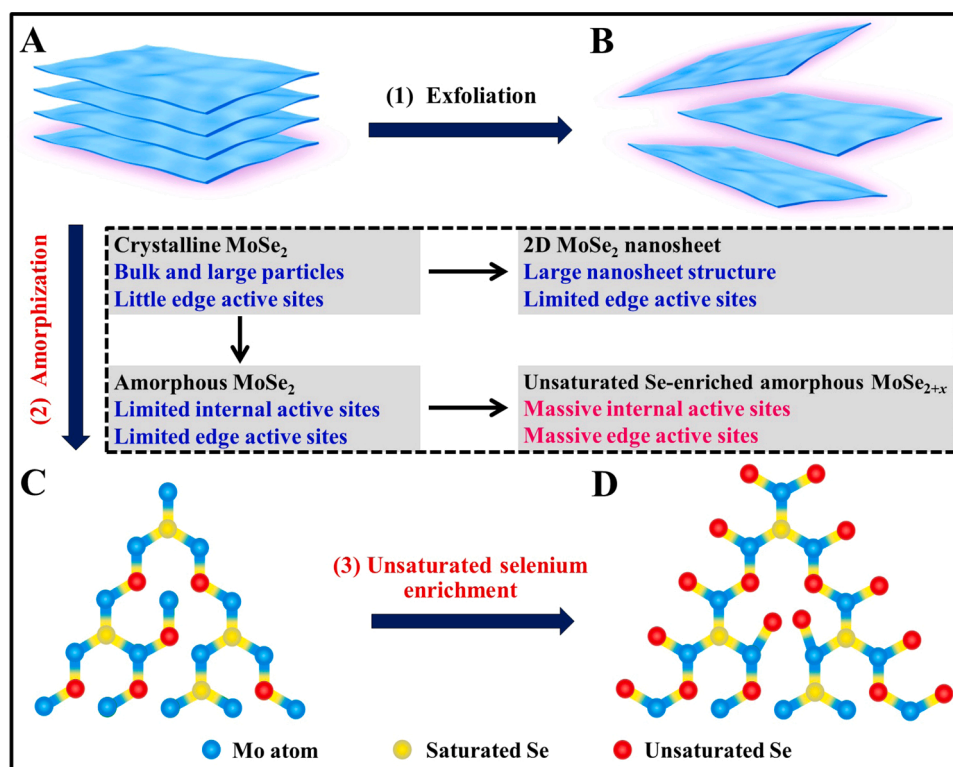
Fig. 1. Schematic illustration for the increasing H_2-evolution active sites by active-site regulation: (1) the traditional exfoliation of bulk $MoSe_2$ into 2D nanosheets (only increasing edge active sites); (2, 3) the novel rich-active-site regulation strategy of (2) amorphization and (3) unsaturated selenium enrichment for $MoSe_{2+x}$ amorphous nanoclusters (with maximized number of unsaturated active Se sites).

(P25) was dispersed in 80 mL of ethanol solution under constant magnetic stirring and then the above system was deoxidized by purging N_2. Next, 156 μL of $MoCl_5$/ethanol (0.1 mol L^{-1}, under argon protection) and 6240 μL of dibenzyl diselenide ($C_{14}H_{14}Se_2$)/ethanol (0.01 mol L^{-1}) solution were introduced into the above suspension by injector (100 μL), where the molar ratio of Se to Mo is controlled to be 8:1. Subsequently, the above mixture was irradiated by the LED lamp ($\lambda = 365$ nm) for 2 h to enable the photoinduced co-reduction synthesis of a-$MoSe_{2+x}$ onto the TiO_2. Finally, the resulting products were filtered and washed with ethanol several times and dried in a vacuum oven (60 °C, 12 h) to obtain unsaturated selenium-enriched a-$MoSe_{2+x}$/TiO_2(3 wt%) sample. For the photocatalytic H_2-evolution experiment, the above fresh precipitate of a-$MoSe_{2+x}$/TiO_2 was directly reused to disperse in ethanol sacrificial reagent (80 mL, 25 vol%), and the subsequent details are displayed in the section of photocatalytic H_2-evolution test. To explore the mass effect of a-$MoSe_{2+x}$ to TiO_2, the mass ratio of Mo/TiO_2 was controlled to be 0, 0.1, 0.5, 1, 3, 5, and 7 wt% and the resultant samples were labeled according to the mass of Mo used per 50 mg of TiO_2. Meanwhile, the influence of the Se/Mo molar ratio on the cocatalytic performance of molybdenum selenide was further explored, as displayed in Fig. S1. From the optimized result, it can be found that when the Se/Mo ratio was settled as 8:1, the generated a-$MoSe_{2+x}$/TiO_2 acquired the optimal photoactivity. Thus, the Se/Mo ratio was fixed as 8:1 for the photoinduced co-reduction synthesis of unsaturated selenium-enriched a-$MoSe_{2+x}$/TiO_2 samples. In addition, control experiments were also cautiously conducted to explore the necessary condition for the effective photoinduced co-reduction synthesis of a-$MoSe_{2+x}$, suggesting the coexisting importance of $MoCl_5$ and dibenzyl diselenide precursors, as exhibited in Table S1.

To further demonstrate the superiority of the unsaturated selenium-enriched a-$MoSe_{2+x}$/TiO_2, the traditional amorphous $MoSe_2$/TiO_2 sample was also prepared (Se/Mo = 2:1) for comparison via the above analogous photoinduced co-reduction route and the as-formed sample was denoted as a-$MoSe_2$/TiO_2. Furthermore, the crystalline c-$MoSe_2$/TiO_2 sample was achieved via high-temperature treatment of amorphous a-$MoSe_2$/TiO_2 (N_2, 500 °C, 5 h), which can be well confirmed by the subsequent XRD results (Fig. 3 A and B).

2.2. Characterization

The crystal phase properties and morphologies for various samples were analyzed with an X-ray diffractometer (Japan) and JSM-7500 F/FESEM, respectively. The TEM and elemental mapping images were obtained via JEM-2100 F/TEM. The elemental content analysis was implemented using ICP-OES. The ultraviolet-visible diffuse reflectance spectra were recorded by using a UV–vis instrument (Japan). The ex-situ X-ray photoelectron spectroscopy was gained by an XPS tester (Mg Kα excitation). The in-situ irradiated XPS spectra were achieved by a Thermo ESCALAB 250Xi instrument with Al Kα X-ray radiation. All the XPS binding energies were calibrated by the adventitious carbon C 1 *s* peak at 284.8 eV. Steady-state PL and TRPL were collected on F-7000 fluorescence spectrophotometer (Japan, Hitachi) and FLS920 fluorescence lifetime spectrophotometer (Edinburgh Instruments, UK), respectively.
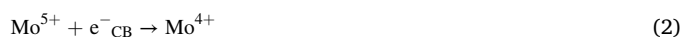
2.3. Photocatalytic H_2 evolution test

The H_2-generation activities were evaluated in a 100 mL Pyrex flask, according to the earlier reported works [34]. In a typical measurement, 0.05 g of the prepared photocatalyst was dispersed in an aqueous solution with the addition of ethanol as the hole scavenger (80 mL, 25 vol %). After purging with nitrogen (0.25 h), the resulting reactant was illuminated by four LED lights (3-W, 365 nm). The evolved hydrogen gas (0.4 mL) was analyzed periodically by gas chromatography (GC-2014 C, Shimadzu Co., Japan, N_2 as carrier gas). For the cycling tests, the above system was re-bubbled with N_2 to evacuate the H_2 products and the

photocatalyst was recycled for the next H_2-generation measurement. Moreover, to evaluate the universality of the unsaturated Se-enriched a-$MoSe_{2+x}$ cocatalyst, the photocatalytic H_2-evolution rates of g-C_3N_4, a-$MoSe_{2+x}$/g-C_3N_4, CdS, and a-$MoSe_{2+x}$/g-C_3N_4 were also tested by using 80 mL of 10 vol% lactic acid as the sacrificial regent.
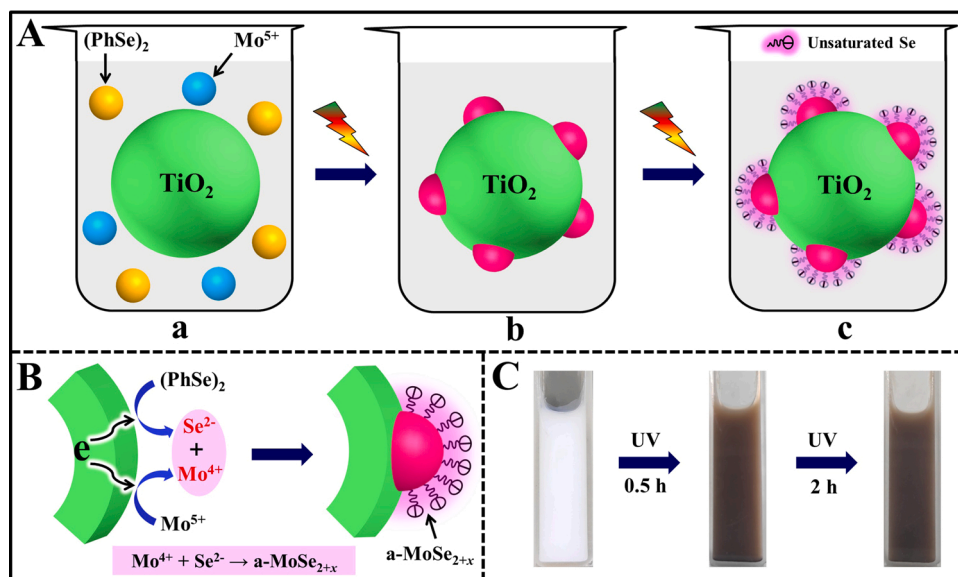
3. Results and discussion

3.1. One-step photoinduced co-reduction synthesis of unsaturated Se-enriched a-$MoSe_{2+x}$/TiO_2

The synthetic strategy of unsaturated selenium-enriched a-$MoSe_{2+x}$/TiO_2 can be schematically illustrated via a mild photoinduced co-reduction route by using $MoCl_5$ and dibenzyl diselenide as the precursors, as shown in Fig. 2. First, $MoCl_5$ and $(PhSe)_2$ (represent dibenzyl diselenide) are successively injected into TiO_2-ethanol suspension under nitrogen protection. In this case, the Mo^{5+} and $(PhSe)_2$ species can be evenly dispersed in the whole reaction system to form TiO_2/Mo^{5+}-$(PhSe)_2$ suspension (Fig. 2A-a), which delivers an essential precursor solution for the generation of unsaturated Se-enriched a-$MoSe_{2+x}$ nanoclusters in the subsequent photoinduced co-reduction process. Under UV-light irradiation, the continuous photoelectrons of TiO_2 can induce the reduction of $(PhSe)_2$ to Se^{2-} ions (Eq. (1)) [35], while the Mo^{5+} can also be effectively reduced to Mo^{4+} due to its positive reduction potential (1.73 V) (Eq. (2), Fig. 2B) [36,37]. Consequently, the produced Se^{2-} can immediately react with Mo^{4+} ions to form the intermediate product of a-$MoSe_{2+x}$ (Fig. 2A-b). With increasing reaction time, the excess $(PhSe)_2$ can further release abundant Se^{2-} to induce the final formation of unsaturated Se-enriched a-$MoSe_{2+x}$ (Eq. (3) [38], Fig. 2A-c). Actually, the enriched Se can not only exist on the surface of a-$MoSe_{2+x}$, but also in its interior, because the amorphous materials are beneficial to regulate their atomic ratios over a wide range (in the whole) [32]. As a result, the color of the above suspension changes from white to brown within 0.5 h, and there is no obvious color change after irradiation for 2 h (Fig. 2 C), indicating the rapid formation process of unsaturated Se-enriched a-$MoSe_{2+x}$. In fact, the successful photoinduced co-reduction synthesis of a-$MoSe_{2+x}$ can be fully proved through the subsequent various characterizations (TEM, XPS et al.). Considering the low-temperature and quick photoinduced co-reduction route, it is rational to determine that the a-$MoSe_{2+x}$ with the amorphous structure and unsaturated selenium-enriched property has been precisely photosynthesized and evenly loaded onto the TiO_2 to form unsaturated selenium-enriched amorphous a-$MoSe_{2+x}$/TiO_2 photocatalyst.

$$(PhSe)_2 + e^-_{CB} \rightarrow Se^{2-} \tag{1}$$

$$Mo^{5+} + e^-_{CB} \rightarrow Mo^{4+} \tag{2}$$

$$Mo^{4+} + Se^{2-} \rightarrow a\text{-}MoSe_{2+x} \tag{3}$$

3.2. Microstructures of unsaturated selenium-enriched a-$MoSe_{2+x}$/TiO_2

To demonstrate the available photoinduced co-reduction synthesis of unsaturated selenium-enriched a-$MoSe_{2+x}$ nanocluster-modified TiO_2, the resultant a-$MoSe_{2+x}$/TiO_2 samples are first characterized via the XRD, FESEM, EDS, and TEM/mapping data. The XRD pattern and FESEM image show that the naked TiO_2 presents the typical diffraction peaks of anatase and rutile (Fig. 3 A) [39] and the aggregated nanoparticles of 30–70 nm (Fig. S2A). After the modification of cocatalysts, all the resultant photocatalysts display the parallel diffraction peaks and morphology relative to unitary TiO_2, suggesting that the mild photoinduced co-reduction route has no effect on the microstructure of TiO_2 (Fig. S2B-D). Notably, the crystalline c-$MoSe_2$/TiO_2(7 wt%) sample emerges a diacritical dominant peak (~31.4°) of drysdallite-2 H $MoSe_2$ (PDF#29–0914) [40], while no XRD peaks of molybdenum selenide can

Fig. 2. (A, B) Illustration for the one-step photoinduced co-reduction synthesis of unsaturated Se-enriched a-MoSe$_{2+x}$/TiO$_2$ photocatalyst: (a) TiO$_2$/Mo^{5+}-(PhSe)$_2$ suspension ((PhSe)$_2$ is dibenzyl diselenide) and the (b) intermediate and (c) final products of a-MoSe$_{2+x}$/TiO$_2$; (C) the corresponding color change of samples in different reaction times.
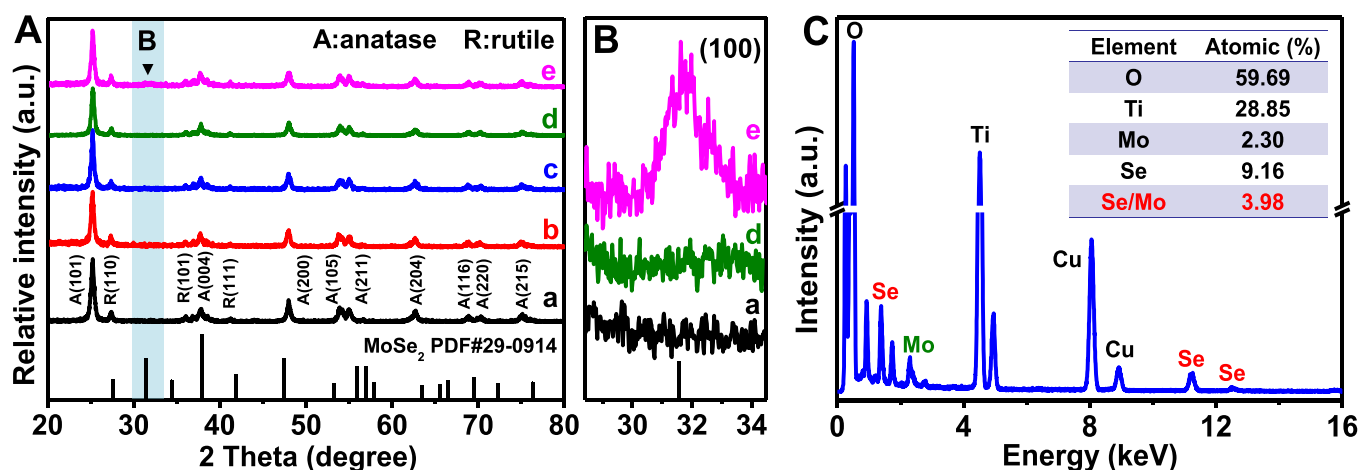
Fig. 3. (A, B) XRD patterns of (a) TiO$_2$, (b) unsaturated selenium-enriched a-MoSe$_{2+x}$/TiO$_2$(3 wt%), (c) conventional amorphous a-MoSe$_2$/TiO$_2$(3 wt%), (d) unsaturated selenium-enriched a-MoSe$_{2+x}$/TiO$_2$(7 wt%), and (e) crystalline c-MoSe$_2$/TiO$_2$(7 wt%); (C) EDX spectrum of unsaturated selenium-enriched a-MoSe$_{2+x}$/TiO$_2$(3 wt%).

be discovered in a-MoSe$_{2+x}$/TiO$_2$(7 wt%) and TiO$_2$ samples (Fig. 3B), implying the amorphous structure of the loaded molybdenum selenide because of the mild and fast photoinduced co-reduction route. In addition, the EDX data of a-MoSe$_{2+x}$/TiO$_2$ exhibits a Se/Mo ratio of 3.98 (Fig. 3 C), forcefully approving the Se-enriched property of the presented a-MoSe$_{2+x}$ due to the massive exposure of unsaturated Se sites (see the XPS results). To obtain more detailed microstructure-information of a-MoSe$_{2+x}$, the TEM/mapping images are displayed in Fig. 4A-C. It can be seen that many small a-MoSe$_{2+x}$ nanoclusters (0.3–1 nm) with the amorphous phase structure (due to the room-temperature photoinduced co-reduction route) are homogenously integrated with the TiO$_2$ photocatalyst (Fig. 4 A, B). In this case, the corresponding EDS/mapping images (Fig. 4 C-C$_5$) show that the Mo and Se signals are uniformly dispersed on the TiO$_2$ surface, further verifying the successful synthesis and homogeneous deposition of a-MoSe$_{2+x}$ nanoclusters. Therefore, the above results distinctly manifest that the a-MoSe$_{2+x}$ nanoclusters with the rich-Se character and amorphous structure have been skillfully synthesized by the one-step photoinduced

co-reduction route.

To further prove the unsaturated selenium-enriched property and the surface chemical state of a-MoSe$_{2+x}$, the ex-situ XPS and ICP-OES characterizations were implemented. Based on the XPS survey spectra (Fig. 5 A), it can be found that all cocatalyst-modified TiO$_2$ photocatalysts show the additional XPS signals of Mo and Se besides the Ti and O peaks compared with pristine TiO$_2$ sample, suggesting the successful integration of molybdenum selenides with TiO$_2$. To fully reveal their chemical states, the corresponding core-level XPS spectra are provided (Fig. 5B-D). Obviously, the high-resolution XPS spectra of Ti 2p in the cocatalyst-loaded samples show the positive movement because of the free-electrons of TiO$_2$ migrate to molybdenum selenide (Fig. 5B). For the core-level XPS spectra of Mo element (Fig. 5 C), the main peaks at 228.7 and 232.1 eV can be ascribed to Mo^{4+} 3$d_{5/2}$ and Mo^{4+} 3$d_{3/2}$, respectively [41–43], while the additional signal peaks at 230.9 and 235.1 eV are attributed to Mo^{5+} 3$d_{5/2}$ and Mo^{5+} 3$d_{3/2}$, respectively (possibly owing to the surface oxidation of molybdenum selenide) [44]. In addition, the detailed microstructure information of unsaturated
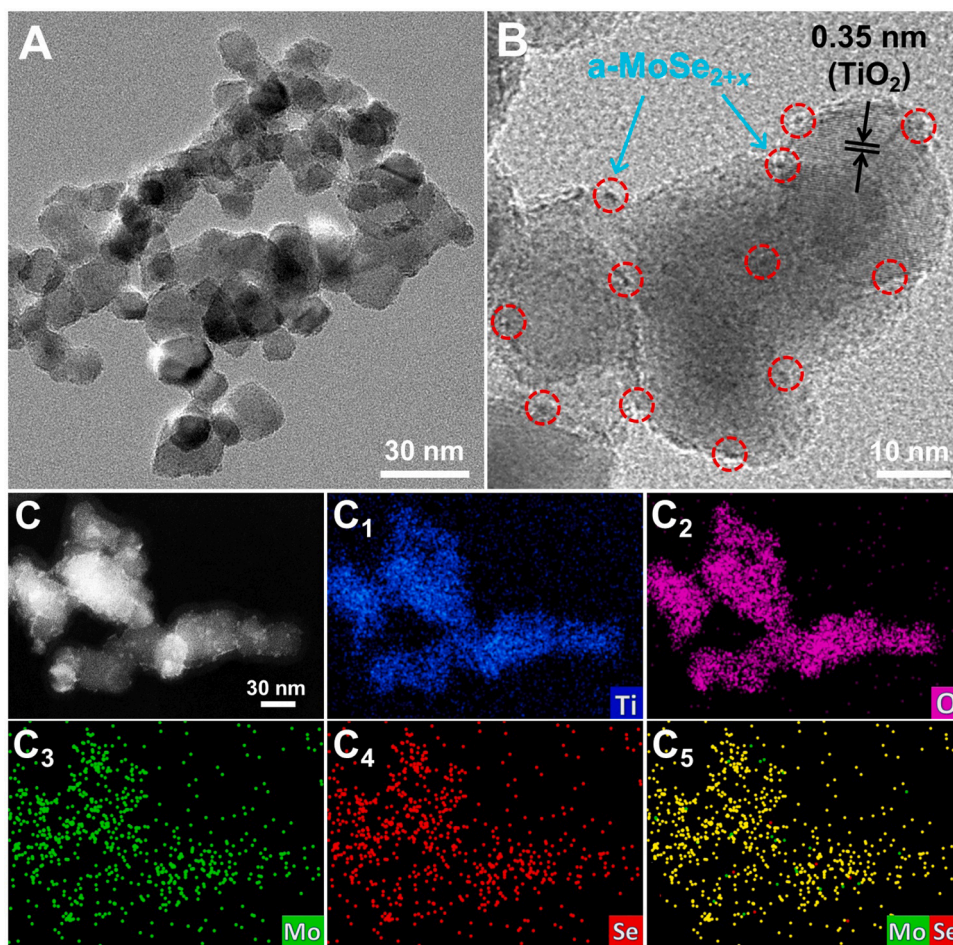
Fig. 4. (A) TEM, (B) HRTEM, (C) HAADF-STEM, and (C$_1$-C$_5$) EDS mapping images of unsaturated Se-enriched a-MoSe$_{2+x}$/TiO$_2$(3 wt%) photocatalyst.

selenium-enriched a-MoSe$_{2+x}$ can be deeply revealed via Se 3d spectra (Fig. 5D). For the crystalline c-MoSe$_2$/TiO$_2$ sample, it can be seen that except a little of unsaturated Se at 52.9 eV (8.1%) [27], there are a large number of saturated Se at 54.6 and 56.2 eV [45]. After amorphizating the c-MoSe$_2$, the as-formed conventional a-MoSe$_2$/TiO$_2$ sample distinctly exhibits an increased amount of unsaturated Se (24.9%) because its amorphous structure is conducive to the exposure of unsaturated Se atoms. It is worth noting that the resultant unsaturated selenium-enriched a-MoSe$_{2+x}$/TiO$_2$ sample presents the highest proportion of unsaturated Se atoms (46.5%) compared with c-MoSe$_2$/TiO$_2$ and a-MoSe$_2$/TiO$_2$ samples, suggesting that the massive unsaturated Se atoms have been effectively incorporated into a-MoSe$_{2+x}$ nanoclusters due to the synergistic promotion for the increase of unsaturated Se by amorphization and unsaturated selenium enrichment. To achieve the actual atom ratios of Se/Mo, the ICP-OES results for different photocatalysts are provided in Table 1. Clearly, compared with c-MoSe$_2$/TiO$_2$ (1.84) and a-MoSe$_2$/TiO$_2$ (2.28), the a-MoSe$_{2+x}$/TiO$_2$ possesses the largest Se/Mo ratio of 3.21 owing to its unsaturated Se-enriched property. Therefore, the above results jointly confirm the successful fabrication of unsaturated Se-enriched MoSe$_{2+x}$ amorphous nanocluster-integrated TiO$_2$ photocatalyst.

The successful preparation of a-MoSe$_{2+x}$ nanoclusters on the TiO$_2$ surface can be further proved by UV–vis diffuse reflectance absorption spectra (Fig. 6) and Raman scattering (Fig. S3). For the UV–vis spectra, it can be found that the unitary TiO$_2$ shows the intrinsic absorption edge at about 390 nm due to its wide band gap structure [46]. After coupling with molybdenum selenide, all the formed photocatalysts exhibit a comparable absorption edge and the enhanced visible-light absorption in 400–800 nm relative to bare TiO$_2$, manifesting that the molybdenum

selenide only loads on the surface of TiO$_2$ and does not change its intrinsic absorption edge. Notably, with increasing the a-MoSe$_{2+x}$ weight, the visible light absorption is progressively increased, while the corresponding sample color is also gradually deepened (inset in Fig. 6), indicating the a-MoSe$_{2+x}$ is controllably deposited onto the TiO$_2$. In addition, in comparison to conventional amorphous a-MoSe$_2$/TiO$_2$(3 wt %) and crystalline c-MoSe$_2$/TiO$_2$(3 wt%), the resultant unsaturated Se-enriched a-MoSe$_{2+x}$/TiO$_2$(3 wt%) displays a stronger visible-light absorption, which may be attributed to the unsaturated Se-enriched feature of a-MoSe$_{2+x}$. The Raman spectra can also provide a convincing evidence for the successful preparation of a-MoSe$_{2+x}$ (Fig. S3). Obviously, three dominant peaks (398 (B$_{1\,g}$), 521 (A$_{1\,g}$), and 633 cm^{-1} (E$_{g(2)}$)) can be found for TiO$_2$ phase. However, compared with the pure TiO$_2$, the peak intensity of TiO$_2$ phase in a-MoSe$_{2+x}$/TiO$_2$ sample clearly decrease, which can be ascribed to the loading of unsaturated Se-enriched MoSe$_{2+x}$ nanoclusters on the TiO$_2$ surface. Noteworthily, a new Raman peak at 260 cm^{-1} is emerged for a-MoSe$_{2+x}$ species, further indicating that the a-MoSe$_{2+x}$ cocatalyst has been effectively prepared and anchored onto the TiO$_2$ photocatalyst via the mild photoinduced co-reduction route.

3.3. Photocatalytic performance and mechanism

Photocatalytic H$_2$ evolution experiments have been performed with different samples under the same conditions and the results are exhibited in Fig. 7. It can be seen that the pristine TiO$_2$ shows a minor H$_2$ evolution performance (46.0 μmol h^{-1} g^{-1}). After loading with crystalline c-MoSe$_2$ to generate c-MoSe$_2$/TiO$_2$, the hydrogen-production rate is slightly improve due to the negligible active-edge-site density of
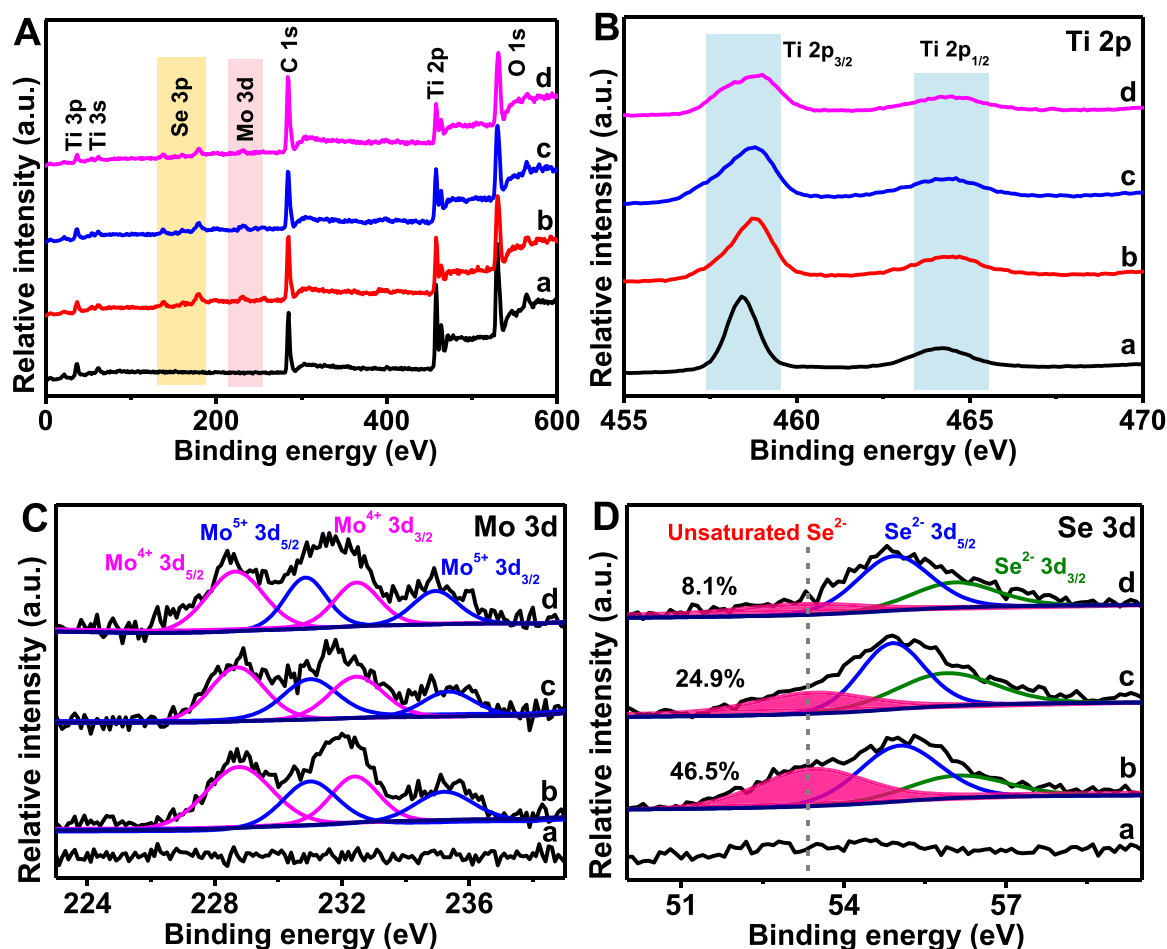
Fig. 5. (A) XPS survey spectra and high-resolution XPS spectra of (B) Ti 2*p*, (C) Mo 3*d*, and (D) Se 3*d* for (a) TiO$_2$, (b) unsaturated Se-enriched a-MoSe$_{2+x}$/TiO$_2$(3 wt %), (c) conventional a-MoSe$_2$/TiO$_2$(3 wt%), and (d) crystalline c-MoSe$_2$/TiO$_2$(3 wt%).

Table 1
The ICP-OES results (atom %) for various samples.

Samples	Se (at%)	Mo (at%)	Se/Mo
TiO$_2$	0	0	0
a-MoSe$_{2+x}$/TiO$_2$(3 wt%)	8.70	2.71	3.21
a-MoSe$_2$/TiO$_2$(3 wt%)	6.06	2.66	2.28
c-MoSe$_2$/TiO$_2$(3 wt%)	4.36	2.37	1.84

unsaturated Se [47]. Meanwhile, amorphous a-MoSe$_2$/TiO$_2$ delivers a further boosted photoactivity for hydrogen generation since the amorphous configuration of a-MoSe$_2$ can provide more defect sites to expose active unsaturated Se centers for interfacial reaction. Noteworthily, after the unsaturated selenium enrichment and amorphization of MoSe$_2$ (to maximal increase of unsaturated Se atoms), the resulting unsaturated Se-enriched amorphous a-MoSe$_{2+x}$/TiO$_2$(3 wt%) demonstrates the maximal activity (4984.46 μmol h^{-1} g^{-1}, AQE = 23.90%, λ = 365 nm, see SI-4 for the calculated details), with the 4.51 and 1.76-fold enhancement relative to that of c-MoSe$_2$/TiO$_2$ and a-MoSe$_2$/TiO$_2$ samples and far superior to that of typical low-cost cocatalyst-modified TiO$_2$ photocatalysts (Table S2). Furthermore, the six intermittent H$_2$-evolution cycles lasting for 36 h indicate the excellent photostability (Fig. 7B, SI-5) and high TON (892.7, SI-6) of a-MoSe$_{2+x}$/TiO$_2$(3 wt%).

The above results intensively suggest that the coupling of unsaturated selenium enrichment and amorphization can collectively increase the active unsaturated Se sites for accelerating the H$_2$-evolution rate of a-MoSe$_{2+x}$/TiO$_2$. Based on this, a rich unsaturated selenium-mediated mechanism is raised (Fig. 8). Early reported results manifest that the
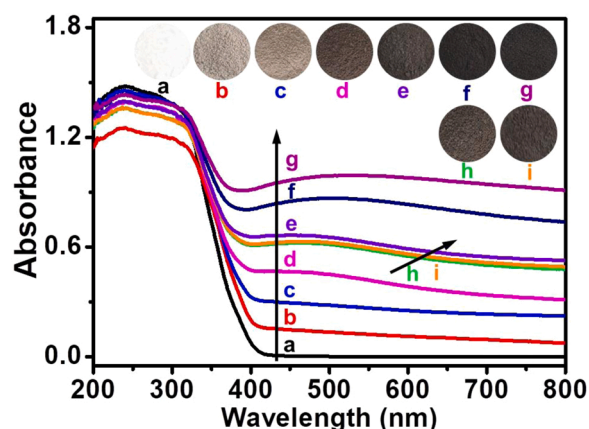

Fig. 6. UV–vis spectra of different photocatalysts: (a) TiO$_2$, (b-g) unsaturated selenium-enriched (b) a-MoSe$_{2+x}$/TiO$_2$(0.1 wt%), (c) a-MoSe$_{2+x}$/TiO$_2$(0.5 wt %), (d) a-MoSe$_{2+x}$/TiO$_2$(1 wt%), (e) a-MoSe$_{2+x}$/TiO$_2$(3 wt%), (f) a-MoSe$_{2+x}$/TiO$_2$(5 wt%), (g) a-MoSe$_{2+x}$/TiO$_2$(7 wt%), (h) conventional amorphous a-MoSe$_2$/TiO$_2$(3 wt%), and (i) crystalline c-MoSe$_2$/TiO$_2$(3 wt%).

unsaturated Se edges on the crystalline MoSe$_2$ can work as excellent active centers to boost the H$_2$ formation [38]. However, the exposed unsaturated Se-edge-sites are quite insufficient owing to its highly ordered lattice array (Fig. 8A-a) [48]. Although the amorphization of crystalline MoSe$_2$ can increase the unsaturated Se sites to a certain extent, the increased number is still very limited (Fig. 8A-b). In this
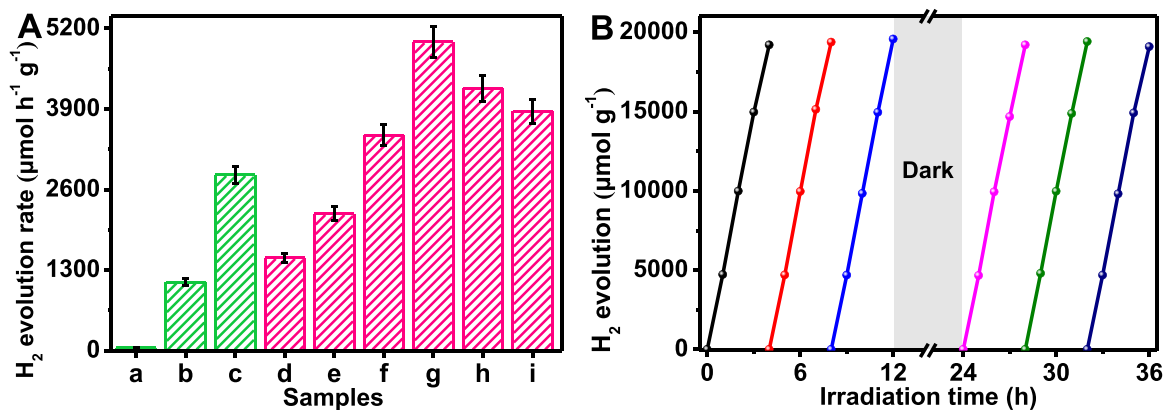
Fig. 7. (A) The photocatalytic H_2-production rates of various samples: (a) TiO_2, (b) crystalline c-$MoSe_2$/TiO_2(3 wt%), (c) conventional amorphous a-$MoSe_2$/TiO_2(3 wt%), and unsaturated selenium-enriched (d) a-$MoSe_{2+x}$/TiO_2(0.1 wt%), (e) a-$MoSe_{2+x}$/TiO_2(0.5 wt%), (f) a-$MoSe_{2+x}$/TiO_2(1 wt%), (g) a-$MoSe_{2+x}$/TiO_2(3 wt%), (h) a-$MoSe_{2+x}$/TiO_2(5 wt%), and (i) a-$MoSe_{2+x}$/TiO_2(7 wt%); (B) Cycling test of unsaturated selenium-enriched a-$MoSe_{2+x}$/TiO_2(3 wt%) sample.
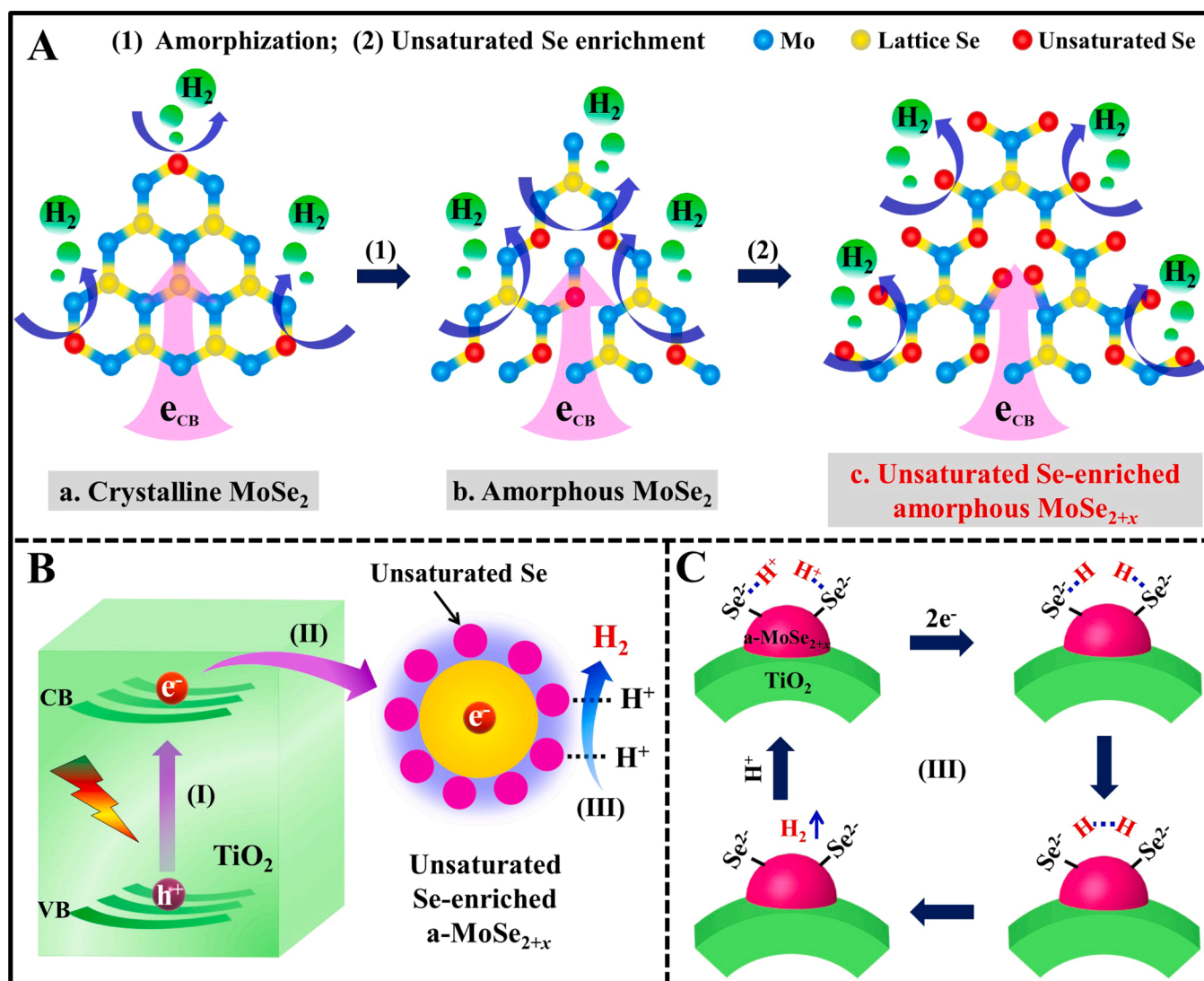

Fig. 8. (A) Cooperation of unsaturated selenium enrichment and amorphization for a-$MoSe_{2+x}$ cocatalyst; (B, C) Proposed rich unsaturated selenium-mediated H_2-evolution mechanism of a-$MoSe_{2+x}$/TiO_2.

study, the unsaturated Se sites in a-$MoSe_{2+x}$ can be maximumly increased by the coupling of unsaturated selenium enrichment and amorphization. As a result, in comparison to the traditional crystalline

$MoSe_2$ cocatalyst (the unsaturated Se only loading on its edges), one of the most advantageous characteristics is that the whole a-$MoSe_{2+x}$ nanoclusters with massive unsaturated selenium sites (both the interior

and edge) can act as the H_2-evolution sites to greatly boost the cocatalytic activity (Fig. 8A-c). Hence, a rich unsaturated selenium-mediated mechanism is displayed as following (Fig. 8B, C). Under irradiation with UV light, the photoelectrons of TiO_2 can be availably excited from the VB to CB (Fig. 8B-(I)) and subsequently are trapped by a-MoSe$_{2+x}$ cocatalyst (Fig. 8B-(II)) to participate in the interface reactions [48]. Meanwhile, the abundant unsaturated Se atoms in the whole a-MoSe$_{2+x}$ nanoclusters can not only provide sufficient proton-adsorption-centers to enrich H^+, but also present an outstanding catalytic efficiency to fleetly convert H^+ to H_2 based on the rich unsaturated selenium-mediated cocatalytic H_2-evolution cycle (Fig. 8B-(III) and C). Hence, the unsaturated Se-rich a-MoSe$_{2+x}$ nanoclusters are identified as the highly active cocatalyst to markedly improve the photocatalytic H_2-evolution efficiency of TiO_2.

To validate the above-raised mechanism, the free energies changes (ΔG_{H*}) for different H-adsorbed states have been calculated and the details/models are displayed in SI-7, Fig. S4, and Fig. 9A-F. For rationalize the calculated results, the (001) surface of $MoSe_2$ was optimized as the typical model because both Mo and Se sites can coexist on this surface. In this case, the Mo (Fig. 9B) and Se (Fig. 9 C) sites present the ΔG_{H*} values of -1.20 and 0.66 eV (Fig. 9 G), respectively, suggesting that the Se site on $MoSe_2$ is responsible for the outstanding catalytic-active-site of H_2 generation, in good agreement with the early reported results [38]. In addition, to fully prove the superiority of active Se-rich environment for the cocatalytic H_2-evolution, the unsaturated Se-enriched $MoSe_2$ model was further simulated by removing one Mo

atom to produce Mo vacancy, as displayed in Fig. 9D and E. It is interesting to find that the ΔG_{H*} of Se site was further reduced to 0.24 eV. In fact, in addition to the Mo-vacancied (001) $MoSe_2$, the above active Se-enriched surrounding can also be mimicried by adhering an excess Se on the Se site (Fig. 9 F) [49]. In this case, the calculated ΔG_{H*} is also decreased (-0.27 eV). All of the above cases suggest that the the active Se-enriched surrounding can not only provide abundant reactive active-centers, but also further strengthen the H_2-evolution efficiency of Se sites by optimizing the ΔG_{H*} towards zero [38]. Therefore, the rich-active-site regulation strategy is a versatile means to boost the interfacial H_2-production reaction of a-MoSe$_{2+x}$, perfectly matched with the raised H_2-evolution mechanism.

The charge transfer dynamics between a-MoSe$_{2+x}$ and TiO_2 is revealed through in-situ irradiated XPS (Fig. 10) and TRPL spectra (Fig. 11 A, Table S3) [50–52]. From Fig. 10A and B, it can be found that after the TiO_2 surface was loaded with a-MoSe$_{2+x}$, the peak positions of Ti 2p and O 1s in the resultant a-MoSe$_{2+x}$/TiO_2 were moved to the higher values in comparison with those of pure TiO_2, suggesting that the electrons transferred from TiO_2 to a-MoSe$_{2+x}$ due to the redistribution of free electrons. Actually, the presented result is rational due to the fact that the work function of a-MoSe$_{2+x}$ (4.35 eV) [53] is bigger than that of TiO_2 (4.20 eV) (Fig. 10C) [44], which can drive the free-electron of TiO_2 transfer to a-MoSe$_{2+x}$ to form the balanced Fermi levels (Fig. 10D). It is noteworthy that when the a-MoSe$_{2+x}$/TiO_2 sample is irradiated with UV-light, the binding energies of Ti 2p and O 1s further increase with reference to those in dark, indicating the photoelectrons of TiO_2 transfer
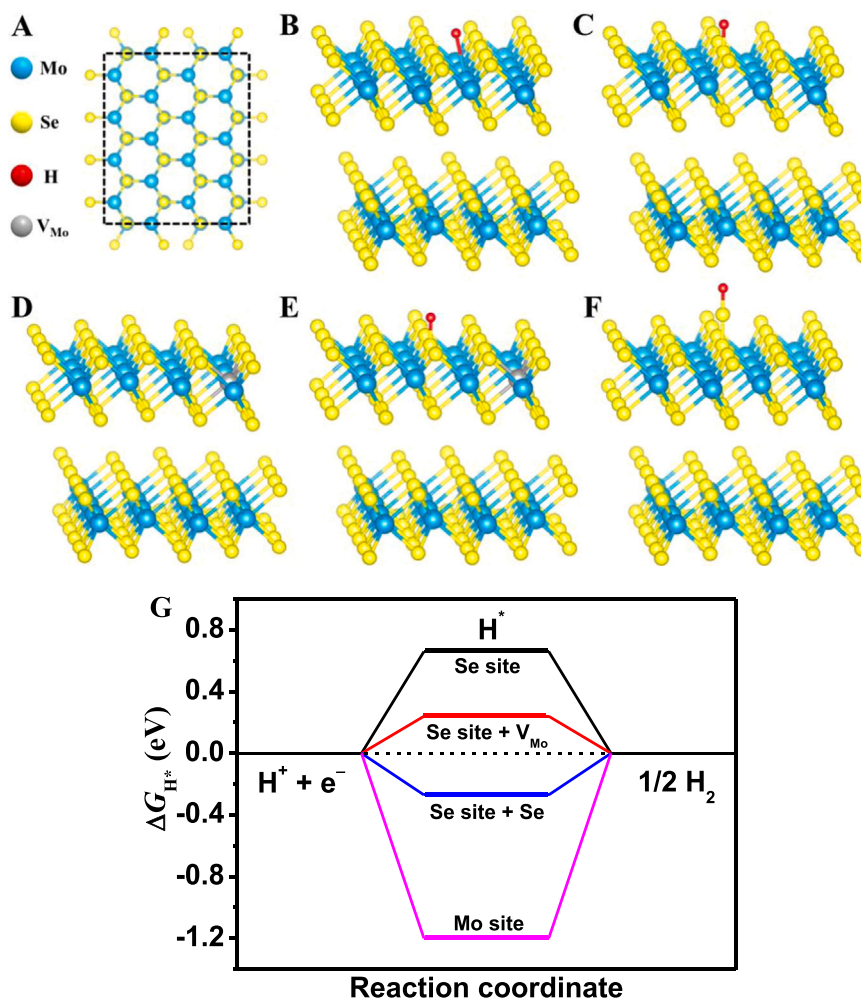
Fig. 9. (A) The structure model of (001) $MoSe_2$ from the top view; (B, C) H adsorption at (B) Mo site and (C) Se site; (D) Mo-vacancy on (001) $MoSe_2$; (E, F) H adsorption at Se site of (001) $MoSe_2$ with (E) Mo-vacancy and (F) Se-adsorption; (G) DFT-calculated adsorption energies for different H-adsorbed states.
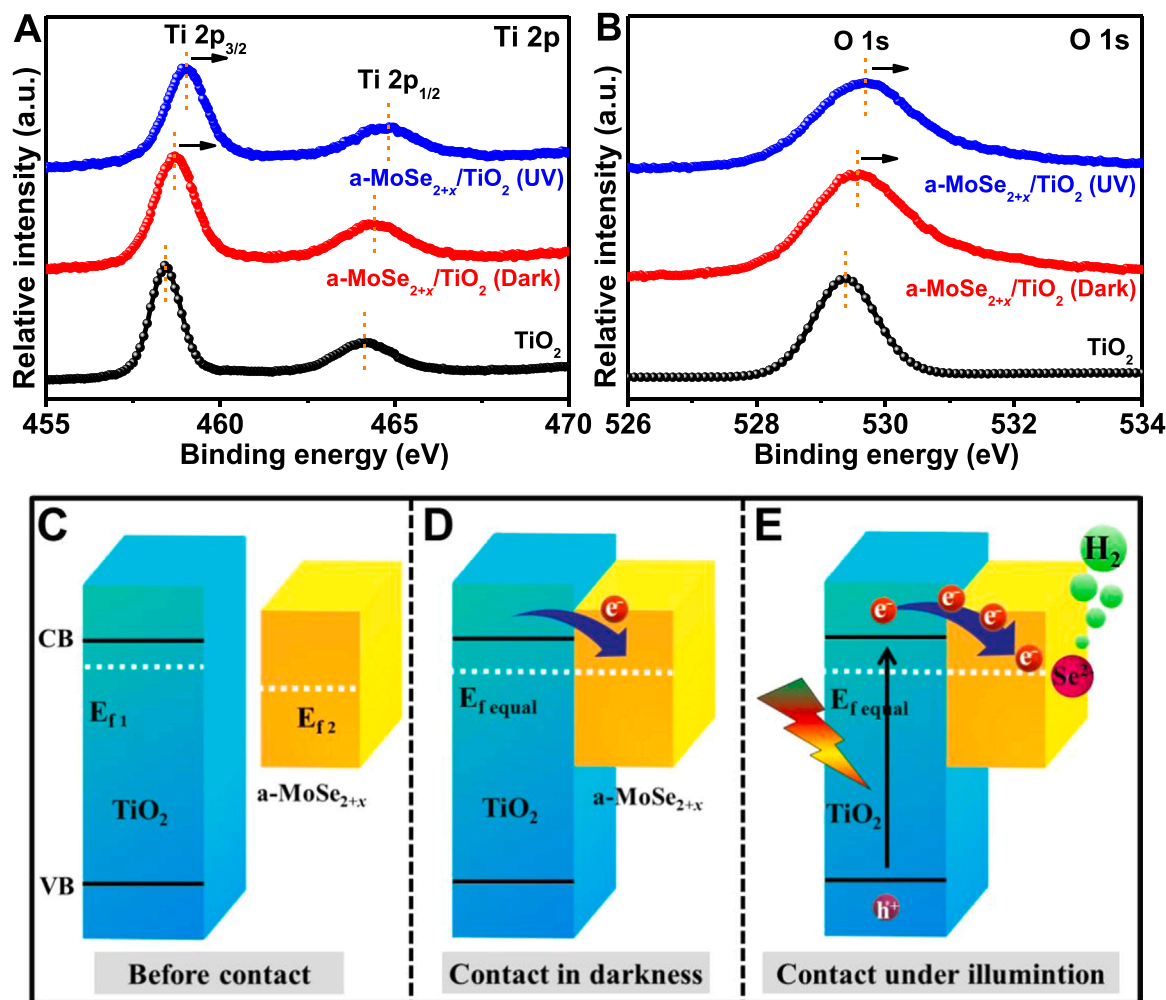
Fig. 10. In situ irradiated XPS results of (A) Ti 2p and (B) O 1s for TiO$_2$, and unsaturated Se-enriched a-MoSe$_{2+x}$/TiO$_2$ in dark and under illumination; (C-E) Illustration of the enhanced electron transfer from TiO$_2$ to unsaturated Se-enriched a-MoSe$_{2+x}$: (C) before and (D) after contact in dark state, and (E) contact under illumintion.

to a-MoSe$_{2+x}$ (Fig. 10E) owing to the excellent photoelectron capture capability of a-MoSe$_{2+x}$. In fact, the above directional transfer of photoelectrons is further proved by the TRPL results (Fig. 11 A). Clearly, the a-MoSe$_{2+x}$/TiO$_2$ sample presents the maximum average fluorescence lifetime ($\tau_{ave} = 9.46$) compared with a-MoSe$_2$/TiO$_2$ ($\tau_{ave} = 9.02$) and c-MoSe$_2$/TiO$_2$ ($\tau_{ave} = 8.63$) samples because of the speedy trapping of photoexcited electrons via a-MoSe$_{2+x}$, which can provide a flow of photoelectrons to participate in the subsequent hydrogen generation process [54]. Thereby, the as-presented analyses directly unravel that the loaded a-MoSe$_{2+x}$ can effectively boost the the interfacial photoelectrons transfer by a-MoSe$_{2+x}$, thus improving the following H$_2$-evolution rate.

To further testify the superior H$_2$-production activity of unsaturated selenium sites and the promoted electron separation and transmission in a-MoSe$_{2+x}$/TiO$_2$, the photoelectrochemical tests have been carried out (SI-8, Fig. 11B-D). Distinctly, the LSV results show that the cathode current density increases gradually in the order of TiO$_2$, crystalline c-MoSe$_2$/TiO$_2$, conventional a-MoSe$_2$/TiO$_2$, and unsaturated selenium-rich a-MoSe$_{2+x}$/TiO$_2$ (Fig. 11B), which can be attributed to the increased number of unsaturated selenium (in accordance with the photoactivity in Fig. 7). The above fact powerfully suggests that the rich unsaturated selenium can greatly reduce the H$_2$-generation overpotential, while accelerating the interfacial hydrogen evolution reaction due to its active site effect [55,56]. In addition, the rapid carrier separation and transfer can be well confirmed via *i-t* (Fig. 11 C) and EIS

results (Fig. 11D). It is clear that compared with the TiO$_2$, c-MoSe$_2$/TiO$_2$ and a-MoSe$_2$/TiO$_2$, the a-MoSe$_{2+x}$/TiO$_2$ sample exhibits the biggest current intensity and smallest impedance radius, indicating the fastest charge separation and transfer in the a-MoSe$_{2+x}$/TiO$_2$ photocatalyst. Thereby, the unsaturated selenium-enriched a-MoSe$_{2+x}$ is a wonderful cocatalyst to not only excellently extract the photoelectrons from TiO$_2$ for improving the separation efficiency of photocarriers, but also facilitate the interfacial catalytic reaction by supplying abundant unsaturated-selenium atoms as H$_2$-evolution active sites.

Versatility is a very important criterion to evaluate the excellent cocatalyst [57–59]. Hence, the universality of a-MoSe$_{2+x}$ cocatalyst was further revealed by depositing a-MoSe$_{2+x}$ on different photocatalysts (such as g-C$_3$N$_4$ and CdS) (SI-1 and 2). Distinctly, all the resultant photocatalysts demonstrate the improved visible-light absorption (Fig. S5) and similar morphology (Fig. S6) compared with the pure g-C$_3$N$_4$ and CdS photocatalysts. In this case, all the a-MoSe$_{2+x}$ cocatalyst-loaded photocatalysts present significantly enhanced hydrogen production performance, forcefully manifesting the generalization of a-MoSe$_{2+x}$ cocatalyst (Fig. 12 A). Furthermore, the presented one-step photoinduced co-reduction route is employed as the versatile means to fabricate representative selenide cocatalysts (SI-3), including a-FeSe$_{1+x}$, a-CoSe$_{1+x}$, a-NiSe$_{1+x}$, a-CuSe$_{1+x}$, and a-WSe$_{2+x}$ (Fig. S7). Clearly (Fig. 12B), all the above cocatalysts can greatly improve the photocatalytic H$_2$-evolution activity of TiO$_2$. Thus, the above results fully reveal the generality of the unsaturated selenium-rich a-MoSe$_{2+x}$
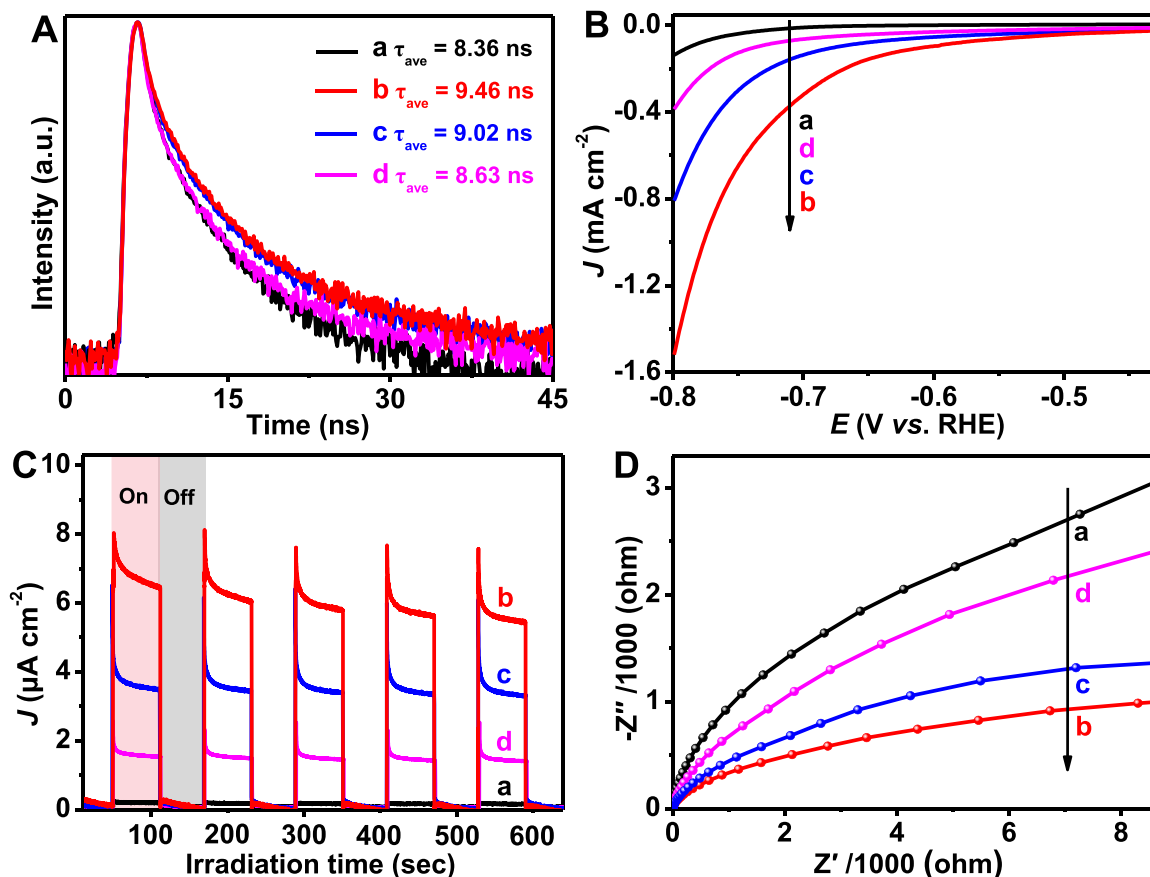
Fig. 11. (A) Transient-state photoluminescence spectra, (B) linear sweep voltammetry curves, (C) transient photocurrent response and (D) electrochemical impedance spectra of (a) TiO_2, (b) unsaturated selenium-rich a-$MoSe_{2+x}$/TiO_2(3 wt%), (c) conventional a-$MoSe_2$/TiO_2(3 wt%), and (d) crystalline c-$MoSe_2$/ TiO_2(3 wt%).

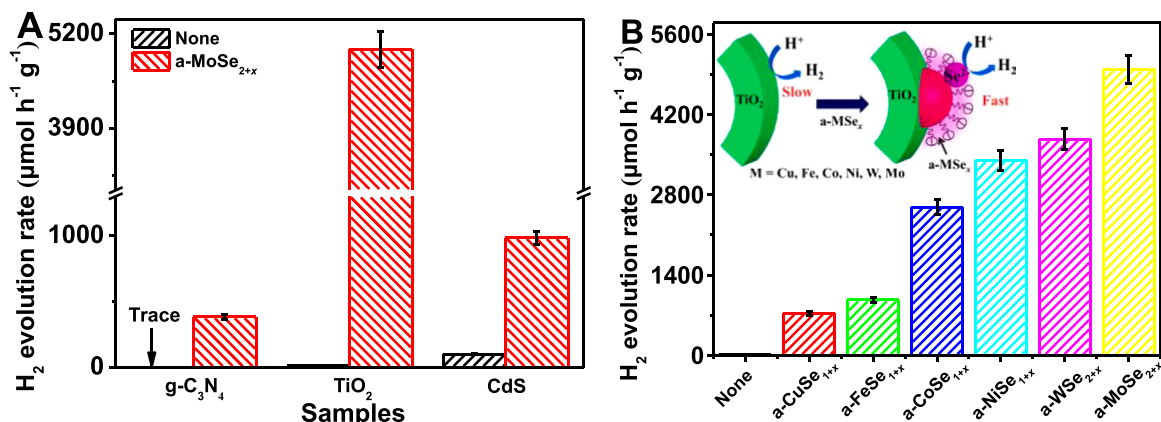**Fig. 12.** (A) Photoactivity of representative photocatalytic materials before and after unsaturated Se-enriched a-$MoSe_{2+x}$ deposition and (B) H_2-generation rates of TiO_2 after loading with other unsaturated Se-enriched selenides.

cocatalyst and the presented one-step photoinduced co-reduction route.

4. Conclusions

In summary, the unsaturated selenium-enriched $MoSe_{2+x}$ amorphous cocatalyst has been firstly designed and constructed via a mild photoinduced co-reduction route by using $MoCl_5$ and dibenzyl diselenide as the precursors. The resultant a-$MoSe_{2+x}$ with the unsaturated selenium-enriched character (46.5%) and small size (0.3 −1 nm) can be uniformly loaded on the TiO_2 surface to prepare unsaturated Se-

enriched a-$MoSe_{2+x}$-modified TiO_2 photocatalyst. Photocatalytic experiments exhibited that the as-formed a-$MoSe_{2+x}$/TiO_2 possesses a superior H_2-evolution activity (4984.46 $\mu mol \ h^{-1} \ g^{-1}$, AQE = 23.90%, λ = 365 nm), which is 4.51 and 1.76 times as high as that of crystalline c-$MoSe_2$/TiO_2 and conventional amorphous a-$MoSe_2$/TiO_2 samples, respectively. Hence, a rich unsaturated Se-mediated H_2-evolution mechanism is proposed, namely, the abundant unsaturated Se atoms as the active sites can not only provide sufficient proton-adsorption-centers to enrich H^+, but also present an outstanding catalytic efficiency to fleetly convert H^+ to H_2. It was worth mentioning that the a-$MoSe_{2+x}$

nanocluster was successfully confirmed to be the general H$_2$-evolution cocatalyst for typical photocatalytic material (such as g-C$_3$N$_4$ and CdS), and the existing one-step photoinduced co-reduction route was extended to fabricate a variety of selenide cocatalysts. This study not only delivers a new insight into the design of active-site-enriched cocatalysts, but also affords a green and facile photoinduced co-reduction route to prepare potential molybdenum selenide cocatalysts for the first time.

CRediT authorship contribution statement

Duoduo Gao: Methodology, Investigation, Data curation, Writing – original draft. **Jiachao Xu:** Visualization. **Feng Chen:** Software. **Ping Wang:** Validation, Project administration. **Huogen Yu:** Conceptualization, Supervision, Resources, Funding acquisition.

Declaration of Competing Interest

The authors declare that they have no known competing financial interests or personal relationships that could have appeared to influence the work reported in this paper.

Acknowledgements

Appendix A. Supporting information

Supplementary data associated with this article can be found in the online version at doi:10.1016/j.apcatb.2021.121053.

References

[1] C. Cheng, B. He, J. Fan, B. Cheng, S. Cao, J. Yu, An inorganic/organic S-scheme heterojunction H$_2$-production photocatalyst and its charge transfer mechanism, Adv. Mater. 33 (2021) 2100317.
[2] J. Jing, J. Yang, Z. Zhang, Y. Zhu, Supramolecular zinc porphyrin photocatalyst with strong reduction ability and robust built-in electric field for highly efficient hydrogen production, Adv. Energy Mater. 11 (2021), 2101392.
[3] Z. Lin, Y. Zhao, J. Luo, S. Jiang, C. Sun, S. Song, Apparent potential difference boosting directional electron transfer for full solar spectrum-irradiated catalytic H$_2$ evolution, Adv. Funct. Mater. 30 (2020), 1908797.
[4] W. Zhong, X. Wu, Y. Liu, X. Wang, J. Fan, H. Yu, Simultaneous realization of sulfur-rich surface and amorphous nanocluster of NiS$_{1+x}$ cocatalyst for efficient photocatalytic H$_2$ evolution, Appl. Catal. B Environ. 280 (2021), 119455.
[5] H. Xu, J.-L. Shi, S. Lyu, X. Lang, Visible-light photocatalytic selective aerobic oxidation of thiols to disulfides on anatase TiO$_2$, Chin. J. Catal. 41 (2020) 1468–1473.
[6] X. Chen, Y. Kuwahara, K. Mori, C. Louis, H. Yamashita, Zoopery study on the treatment of intracranial aneurysms with a new blood flow guide device, J. Mater. Chem. A 9 (2021) 2815–2821.
[7] X. Lu, W. Chen, Y. Yao, X. Wen, J.N. Hart, C. Tsounis, C. Ying Toe, J. Scott, Y.H. Ng, Photogenerated charge dynamics of CdS nanorods with spatially distributed MoS$_2$ for photocatalytic hydrogen generation, Chem. Eng. J. 420 (2021), 127709.
[8] Z. Xu, X. Deng, Y. Chen, J. Wen, L. Shi, Z. Bian, Engineering a rapid charge transfer pathway for enhanced photocatalytic removal efficiency of hexavalent chromium over C$_3$N$_4$/NH$_2$–UIO-66 compounds, Sol. RRL 5 (2021), 2000416.
[9] C. Bie, H. Yu, B. Cheng, W. Ho, J. Fan, J. Yu, Design, fabrication, and mechanism of nitrogen-doped graphene-based photocatalyst, Adv. Mater. 33 (2021), 2003521.
[10] R. Shen, Y. Ding, S. Li, P. Zhang, Q. Xiang, Y.H. Ng, X. Li, Constructing low-cost Ni$_3$C/twin-crystal Zn$_{0.5}$Cd$_{0.5}$S heterojunction/homojunction nanohybrids for efficient photocatalytic H$_2$ evolution, Chin. J. Catal. 42 (2021) 25–36.
[11] X. Li, J. Liu, J. Huang, C. He, F. Deng, All organic S-scheme heterojunction PDI-Ala/S-C$_3$N$_4$ photocatalyst with enhanced photocatalytic performance, Acta Phys. Chim. Sin. 6 (2021), 2010030, 2010030-0.
[12] J. Hao, D. Yang, J. Wu, B. Ni, L. Wei, Q. Xu, Y. Min, H. Li, Utilizing new metal phase nanocomposites deep photocatalytic conversion of CO$_2$ to C$_2$H$_4$, Chem. Eng. J. 423 (2021) 130190.
[13] K. Li, S. Zhang, Y. Li, J. Fan, K. Lv, MXenes as noble-metal-alternative co-catalysts in photocatalysis, Chin. J. Catal. 42 (2021) 3–14.
[14] D. Gao, J. Xu, L. Wang, B. Zhu, H. Yu, J. Yu, Optimizing atomic hydrogen desorption of sulfur-rich NiS$_{1+x}$ cocatalyst for boosting photocatalytic H$_2$ evolution, Adv. Mater. (2022), https://doi.org/10.1002/adma.202108475.
[15] H. He, J. Cao, M. Guo, H. Lin, J. Zhang, Y. Chen, S. Chen, Distinctive ternary CdS/Ni$_2$P/g-C$_3$N$_4$ composite for overall water splitting: Ni$_2$P accelerating separation of photocarriers, Appl. Catal. B Environ. 249 (2019) 246–256.
[16] T. Di, L. Zhang, B. Cheng, J. Yu, J. Fan, CdS nanosheets decorated with Ni@graphene core-shell cocatalyst for superior photocatalytic H$_2$ production, J. Mater. Sci. Technol. 56 (2020) 170–178.
[17] X. Lu, C.Y. Toe, F. Ji, W. Chen, X. Wen, R.J. Wong, J. Seidel, J. Scott, J.N. Hart, Y. H. Ng, Light-induced formation of MoO$_x$S$_y$ clusters on CdS nanorods as cocatalyst for enhanced hydrogen evolution, ACS Appl. Mater. Interfaces 12 (2020) 8324–8332.
[18] D. Ren, Z. Liang, Y.H. Ng, P. Zhang, Q. Xiang, X. Li, Strongly coupled 2D–2D nanojunctions between P-doped Ni$_2$S (Ni$_2$SP) cocatalysts and CdS nanosheets for efficient photocatalytic H$_2$ evolution, Chem. Eng. J. 390 (2020), 124496.
[19] D. Gao, W. Zhong, Y. Liu, H. Yu, J. Fan, Synergism of tellurium-rich structure and amorphization of NiTe$_{1+x}$ nanodots for efficient photocatalytic H$_2$-evolution of TiO$_2$, Appl. Catal. B Environ. 290 (2021), 120057.
[20] J. Wen, L. Ling, Y. Chen, Z. Bian, Pyroelectricity effect on photoactivating palladium nanoparticles in PbTiO$_3$ for Suzuki coupling reaction, Chin. J. Catal. 41 (2020) 1674–1681.
[21] Y. Kuwahara, Y. Fujie, T. Mihogi, H. Yamashita, Hollow mesoporous organosilica spheres encapsulating PdAg nanoparticles and Poly(Ethyleneimine) as reusable catalysts for CO$_2$ hydrogenation to formate, ACS Catal. 10 (2020) 6356–6366.
[22] M. Ahmad, X. Quan, S. Chen, H. Yu, Z. Zeng, Operating redox couple transport mechanism for enhancing photocatalytic H$_2$ generation of Pt and CrO$_x$-decorated ZnCdS nanocrystals, Appl. Catal. B Environ. 283 (2021), 119601.
[23] L. Cheng, H. Yin, C. Cai, J. Fan, Q. Xiang, Single Ni atoms anchored on porous few-layer g-C$_3$N$_4$ for photocatalytic CO$_2$ reduction: The role of edge confinement, Small 16 (2020), 2002411.
[24] S. Anantharaj, S. Kundu, S. Noda, Progress in nickel chalcogenide electrocatalyzed hydrogen evolution reaction, J. Mater. Chem. A 8 (2020) 4174–4192.
[25] Y. Choi, H.-i Kim, G.-h Moon, S. Jo, W. Choi, Boosting up the low catalytic activity of silver for H$_2$ production on Ag/TiO$_2$ photocatalyst: Thiocyanate as a selective modifier, ACS Catal. 6 (2016) 821–828.
[26] H. Shu, D. Zhou, F. Li, D. Cao, X. Chen, Defect engineering in MoSe$_2$ for the hydrogen evolution reaction: From point defects to edges, ACS Appl. Mater. Interfaces 9 (2017) 42688–42698.
[27] D. Gao, B. Zhao, F. Chen, H. Yu, J. Fan, J. Yu, Selenium-rich configuration and amorphization for synergistically maximizing the active-center amount of CoSe$_{1+x}$ nanodots toward efficient photocatalytic H$_2$ evolution, ACS Sustain. Chem. Eng. 9 (2021) 8653–8662.
[28] K. Wang, Z. Xing, D. Meng, S. Zhang, Z. Li, K. Pan, W. Zhou, Hollow MoSe$_2$@Bi$_2$S$_3$/CdS core-shell nanostructure as dual Z-scheme heterojunctions with enhanced full spectrum photocatalytic-photothermal performance, Appl. Catal. B Environ. 281 (2021), 119482.
[29] Z. Lei, S. Xu, P. Wu, Ultra-thin and porous MoSe$_2$ nanosheets: Facile preparation and enhanced electrocatalytic activity towards the hydrogen evolution reaction, Phys. Chem. Chem. Phys. 18 (2016) 70–74.
[30] D. Gao, X. Wu, P. Wang, H. Yu, B. Zhu, J. Fan, J. Yu, Selenium-enriched amorphous NiSe$_{1+x}$ nanoclusters as a highly efficient cocatalyst for photocatalytic H$_2$ evolution, Chem. Eng. J. 408 (2021), 127230.
[31] K. Chang, H. Pang, X. Hai, G. Zhao, H. Zhang, L. Shi, F. Ichihara, J. Ye, Ultra-small freestanding amorphous molybdenum sulfide colloidal nanodots for highly efficient photocatalytic hydrogen evolution reaction, Appl. Catal. B Environ. 232 (2018) 446–453.
[32] C. Guo, Y. Shi, S. Lu, Y. Yu, B. Zhang, Amorphous nanomaterials in electrocatalytic water splitting, Chin. J. Catal. 42 (2021) 1287–1296.
[33] S. Min, Y. Lei, H. Sun, J. Hou, F. Wang, E. Cui, S. She, Z. Jin, J. Xu, X. Ma, Amorphous WS$_x$ as an efficient cocatalyst grown on CdS nanoparticles via photochemical deposition for enhanced visible-light-driven hydrogen evolution, Mol. Catal. 440 (2017) 190–198.
[34] D. Gao, J. Xu, H. Yu, Y. Liu, J. Yu, Hydroxyl-enriched highly crystalline TiO$_2$ suspensible photocatalyst: Facile synthesis and superior H$_2$-generation activity, Chem. Commun. 57 (2021) 2025–2028.
[35] W. Cao, X. Zhang, X. Miao, Z. Yang, H. Xu, γ-Ray-responsive supramolecular hydrogel based on a diselenide-containing polymer and a peptide, Angew. Chem. Int. Ed. 52 (2013) 6233–6237.
[36] J. Światowska-Mrowiecka, S. de Diesbach, V. Maurice, S. Zanna, L. Klein, E. Briand, I. Vickridge, P. Marcus, Li-ion intercalation in thermal oxide thin films of MoO$_3$ as studied by XPS, RBS, and NRA, J. Phys. Chem. C. 112 (2008) 11050–11058.
[37] K.M. Sancier, T. Dozono, H. Wise, ESR spectra of metal oxide catalysts during propylene oxidation, J. Catal. 23 (1971) 270–280.
[38] I.S. Kwon, I.H. Kwak, T.T. Debela, H.G. Abbas, Y.C. Park, J.-P. Ahn, J. Park, H. S. Kang, Se-rich MoSe$_2$ nanosheets and their superior electrocatalytic performance for hydrogen evolution reaction, ACS Nano 14 (2020) 6295–6304.
[39] H. Yu, R. Yuan, D. Gao, Y. Xu, J. Yu, Ethyl acetate-induced formation of amorphous MoS$_x$ nanoclusters for improved H$_2$-evolution activity of TiO$_2$ photocatalyst, Chem. Eng. J. 375 (2019) 121934.
[40] X. Wang, X. Wang, J. Huang, S. Li, A. Meng, Z. Li, Interfacial chemical bond and internal electric field modulated Z-scheme S$_v$-ZnIn$_2$S$_4$/MoSe$_2$ photocatalyst for efficient hydrogen evolution, Nat. Commun. 12 (2021) 4112.
[41] M.A. Mushtaq, M. Arif, X. Fang, G. Yasin, W. Ye, M. Basharat, B. Zhou, S. Yang, S. Ji, D. Yan, Photoelectrochemical reduction of N$_2$ to NH$_3$ under ambient conditions through hierarchical MoSe$_2$@g-C$_3$N$_4$ heterojunctions, J. Mater. Chem. A 9 (2021) 2742–2753.

[42] E.D. Koutsouroubi, I. Vamvasakis, M.G. Minotaki, I.T. Papadas, C. Drivas, S. A. Choulis, G. Kopidakis, S. Kennou, G.S. Armatas, Ni-doped MoS$_2$ modified graphitic carbon nitride layered hetero-nanostructures as highly efficient photocatalysts for environmental remediation, Appl. Catal. B Environ. 297 (2021), 120419.

[43] X. Meng, J. Yang, S. Xu, C. Zhang, B. Ma, Y. Ding, Integrating Mo$_2$B$_x$ (x = 1, 4) with CdS for efficient photocatalytic hydrogen production, Chem. Eng. J. 410 (2021), 128339.

[44] D. Gao, R. Yuan, J. Fan, X. Hong, H. Yu, Highly efficient S^{2-}-adsorbed MoS$_x$-modified TiO$_2$ photocatalysts: A general grafting strategy and boosted interfacial charge transfer, J. Mater. Sci. Technol. 56 (2020) 122–132.

[45] L. Ju, M. Bie, X. Tang, J. Shang, L. Kou, Janus WSSe monolayer: An excellent photocatalyst for overall water splitting, ACS Appl. Mater. Interfaces 12 (2020) 29335–29343.

[46] X. Li, J. Xiong, Y. Xu, Z. Feng, J. Huang, Defect-assisted surface modification enhances the visible light photocatalytic performance of g-C$_3$N$_4$@C-TiO$_2$ direct Z-scheme heterojunctions, Chin. J. Catal. 40 (2019) 424–433.

[47] N. Masurkar, N.K. Thangavel, L.M.R. Arava, CVD-grown MoSe$_2$ nanoflowers with dual active sites for efficient electrochemical hydrogen evolution reaction, ACS Appl. Mater. Interfaces 10 (2018) 27771–27779.

[48] Z. Liang, R. Shen, Y.H. Ng, P. Zhang, Q. Xiang, X. Li, A review on 2D MoS$_2$ cocatalysts in photocatalytic H$_2$ production, J. Mater. Sci. Technol. 56 (2020) 89–121.

[49] F. Wang, Y. Li, T.A. Shifa, K. Liu, F. Wang, Z. Wang, P. Xu, Q. Wang, J. He, Selenium-enriched nickel selenide nanosheets as a robust electrocatalyst for hydrogen generation, Angew. Chem. Int. Ed. 55 (2016) 6919–6924.

[50] M. Sayed, F. Xu, P. Kuang, J. Low, S. Wang, L. Zhang, J. Yu, Sustained CO$_2$-photoreduction activity and high selectivity over Mn, C-codoped ZnO core-triple shell hollow spheres, Nat. Commun. 12 (2021) 4936.

[51] J. He, P. Lyu, B. Jiang, S. Chang, H. Du, J. Zhu, H. Li, A novel amorphous alloy photocatalyst (NiB/In$_2$O$_3$) composite for sunlight-induced CO$_2$ hydrogenation to HCOOH, Appl. Catal. B Environ. 298 (2021), 120603.

[52] Z. Zhang, X. Chen, H. Zhang, W. Liu, W. Zhu, Y. Zhu, A highly crystalline perylene imide polymer with the robust built-in electric field for efficient photocatalytic water oxidation, Adv. Mater. 32 (2020), 1907746.

[53] Q. Zhang, Y. Chen, C. Zhang, C.-R. Pan, M.-Y. Chou, C. Zeng, C.-K. Shih, Bandgap renormalization and work function tuning in MoSe$_2$/hBN/Ru(0001) heterostructures, Nat. Commun. 7 (2016) 13843.

[54] J. Xu, W. Zhong, H. Yu, X. Hong, J. Fan, J. Yu, Triethanolamine-assisted photodeposition of non-crystalline Cu$_x$P nanodots for boosting photocatalytic H$_2$ evolution of TiO$_2$, J. Mater. Chem. C. 8 (2020) 15816–15822.

[55] X. Liu, Y. Zhao, X. Yang, Q. Liu, X. Yu, Y. Li, H. Tang, T. Zhang, Porous Ni$_5$P$_4$ as a promising cocatalyst for boosting the photocatalytic hydrogen evolution reaction performance, Appl. Catal. B Environ. 275 (2020), 119144.

[56] T. Zhong, Z. Yu, R. Jiang, J. Huang, Y. Hou, J. Chen, Y. Zhang, H. Zhu, B. Wang, L. Ding, Activation strategy of WS$_2$ as an efficient photocatalytic hydrogen evolution cocatalyst through Co^{2+} doping to adjust the highly exposed active (100) facet, Sol. RRL 5 (2021), 2100223.

[57] L. Tian, S. Min, Y. Lei, S. Chen, F. Wang, Vanadium carbide: An efficient, robust, and versatile cocatalyst for photocatalytic hydrogen evolution under visible light, Chem. Commun. 55 (2019) 6870–6873.

[58] Q. Zhu, Z. Xu, B. Qiu, M. Xing, J. Zhang, Emerging cocatalysts on g-C$_3$N$_4$ for photocatalytic hydrogen evolution, Small 17 (2021), 2101070.

[59] J. He, W. Zhong, Y. Xu, H. Yu, J. Fan, J. Yu, Few-layered Mo$_x$W$_{1-x}$S$_2$-modified CdS photocatalyst: One-step synthesis with bifunctional precursors and improved H$_2$-evolution activity, Sol. RRL 5 (2021), 2100387.